

<https://doi.org/10.1038/s43247-025-02835-8>

# Vertical structure of chlorophyll-a during marine heatwaves in the California Current Ecosystem

Check for updates

Jian Li<sup>1,2,3</sup>, Arthur J. Miller<sup>1,2</sup>, Qi Wang<sup>4</sup>, Dillon J. Amaya<sup>1,5</sup>, Peiliang Li<sup>1,3,6</sup>, Yanzhen Gu<sup>1,3,6</sup>✉ & Peng Bai<sup>1,7</sup>✉

In the past decades, the California Current Ecosystem has experienced intense marine heatwaves, which have induced significant disruptions to local phytoplankton communities. Here, using 30-year cruise observations, we identify a previously undocumented vertical structure in chlorophyll-a concentration response to marine heatwaves, characterized by reductions in the surface layer coupled with increases in the subsurface. By integrating observations and coupled physical-biogeochemical model products, we demonstrate that declines of surface chlorophyll-a are primarily attributed to suppressed nutrient upwelled to the upper ocean. Although surface irradiance increased modestly (+3.5%), light availability in the subsurface layer improved substantially (+21.7%) due to reduced phytoplankton shading at the surface. Concurrent with enhanced lateral nutrient transport, phytoplankton growth at depth was promoted during heatwave events. This study highlights the pivotal role of subsurface phytoplankton dynamics in shaping the vertical chlorophyll-a concentration structure and its variability under extreme events.

Marine heatwaves (MHWs), defined as prolonged episodes of anomalously warm seawater temperature<sup>1,2</sup>, have shown increasing frequency and intensity over the past century and are projected to intensify further under global climate change<sup>3,4</sup>. Accumulating evidence demonstrates that these extreme events exert cascading impacts on marine ecosystems, including mass coral bleaching<sup>5</sup>, critical habitat degradation<sup>6</sup>, ecosystem regime shifts<sup>7</sup> and unprecedented biodiversity loss<sup>8</sup>. Moreover, MHWs are increasingly being examined along with concurrently occurring biogeochemical extremes<sup>9</sup>, such as acidity and hypoxia<sup>10–12</sup>, which can exacerbate the responses of sensitive marine organisms<sup>12,13</sup>. Such ecological disruptions fundamentally compromise the provision of essential ecosystem services<sup>14</sup>. Given their escalating frequency, unpredictable spatiotemporal patterns, and potentially irreversible ecological consequences, MHWs have emerged as a pressing global concern<sup>14–16</sup>.

As the foundation of marine primary production, phytoplankton regulate key biogeochemical processes, including carbon sequestration, nutrient cycling, and food web dynamics<sup>17,18</sup>. Their biomass and community structures can be significantly influenced by MHWs due to their various sensitivities to thermal anomalies, with cascading effects on productivity and functional diversity<sup>19,20</sup>. Previous studies demonstrated that MHWs

exert spatially heterogeneous impacts on phytoplankton across regions and events<sup>21,22</sup>. Generally, surface chlorophyll-a concentration (CHL) decreases in the tropics and mid-latitudes while it increases at high latitudes during MHWs<sup>23</sup>, with these patterns governed by alterations in nutrient dynamics<sup>21,24,25</sup>, light availability<sup>22</sup>, and iron limitation<sup>26</sup>. Concurrently, phytoplankton community structures tend to exhibit a universal shift toward smaller species during MHWs, altering energy transfer efficiency through marine food webs<sup>24,27–29</sup>.

The California Current Ecosystem (CCE), where CalCOFI (The California Cooperative Oceanic Fisheries Investigations; Fig. 1) is located, experienced multiple severe MHWs in recent decades, driven by synergistic atmospheric-oceanic forcing mechanisms including intensified North Pacific High variations<sup>30,31</sup>, reduced coastal upwelling<sup>32</sup>, and anomalous poleward current transport<sup>33</sup>. Therefore, a growing body of research has documented MHW-induced impacts on phytoplankton within CCE. For example, during the 2014–2015 MHW, often called “the Blob”, suppressed upwelling and intensified stratification reduced the nutrient supply to the euphotic zone, causing significant declines in phytoplankton biomass and net primary production in CCE<sup>34</sup>. Meanwhile, to adapt to the abnormal temperature and nutrient conditions, the phytoplankton community

<sup>1</sup>Ocean College, Zhejiang University, Zhoushan, China. <sup>2</sup>Scripps Institution of Oceanography, University of California, San Diego, La Jolla, USA. <sup>3</sup>Hainan Institute, Zhejiang University, Sanya, China. <sup>4</sup>Marine Academy of Zhejiang Province, Hangzhou, China. <sup>5</sup>NOAA/Physical Sciences Laboratory, Boulder, CO, USA. <sup>6</sup>Hainan Observation and Research Station of Ecological Environment and Fishery Resource in Yazhou Bay, Sanya, China. <sup>7</sup>Marine Science and Technology College, Zhejiang Ocean University, Zhoushan, China. ✉e-mail: [guyanzhen@zju.edu.cn](mailto:guyanzhen@zju.edu.cn); [pengbai@zjou.edu.cn](mailto:pengbai@zjou.edu.cn)

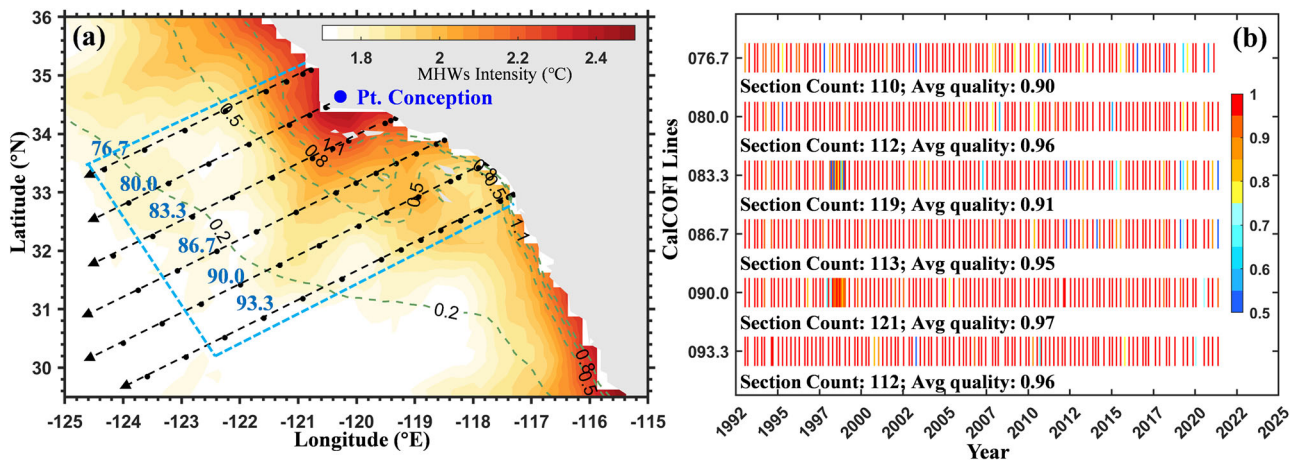


**Fig. 1 | MHWs in the CCE and data records of the CalCOFI.** (a) Mean MHW intensity based on OISST from 1993 to 2022. Black dots and dashes represent the sampling stations and transect lines of CalCOFI cruises. Green dashes represent the

mean surface CHL concentration from Copernicus-GlobColour (1997–2022). Blue box denotes the boundary of the CalCOFI region. (b) Sampling records and their data quality (proportion of valid data) of six CalCOFI Lines from 1993 to 2022.

shifted toward smaller cells<sup>27,35,36</sup>, and harmful algal bloom events in near-shore areas were also related to MHWs<sup>37,38</sup>.

Increasing evidence indicates that MHWs are not confined to the surface layer but may extend to deeper waters<sup>9,39</sup>, with potentially increased duration and intensity in some cases<sup>40,41</sup>. Therefore, vertically propagating extremes represent an emerging topic in recent MHW research<sup>11,13</sup>. These studies revealed that the subsurface compound events (MHW, low oxygen, and high acidity) are often associated with vertical displacements of water masses, have shown significant intensification in recent decades<sup>13</sup>, and are projected to be enhanced under global warming<sup>11</sup>. However, the vertical response of phytoplankton communities to MHWs remains relatively understudied due to limited data availability<sup>42,43</sup>. Recent findings by ref. 43 have highlighted a pronounced decoupling between surface and subsurface phytoplankton biomass during the past decade of ocean warming in the Sargasso Sea. That study underscores the limitations of remote sensing observations and emphasizes the critical role of vertical structures in examining biogeochemical responses to extreme events.

Such vertical decoupling raises critical questions about the underlying mechanisms and whether they differ during short-term extreme events like MHWs compared to gradual, long-term ocean warming. In predominantly nutrient-limited systems like the CCE, the vertical structure of CHL exerts a more critical influence on marine biogeochemical cycling and carbon export potential than surface CHL alone<sup>44</sup>. However, our current understanding of MHW impacts on CHL remains disproportionately focused on epipelagic phytoplankton responses, leaving critical knowledge gaps regarding vertical heterogeneity in phytoplankton dynamics during extreme warming events, thereby hindering our ability to predict ecosystem resilience and climate feedback mechanisms.

In this study, we observed a previously undocumented phenomenon in the CalCOFI region that the vertical response of CHL to MHWs is not uniform, but exhibits a distinct vertical structure characterized by negative surface anomalies overlying positive subsurface anomalies (Herein, we define the “surface” as extending from the sea surface to the subsurface chlorophyll maximum layer (SCML) depth, and the “subsurface” as the water column beneath the SCML depth). Using in situ observations from CalCOFI, we systematically characterize the vertical CHL anomaly structure and associated environmental conditions during MHWs. We further employ physical (PHY) and biogeochemical (BGC) model outputs from the Copernicus Marine Environment Monitoring Service (CMEMS) to investigate the underlying mechanisms driving this vertical pattern. This study aims to advance our understanding of the vertical response of phytoplankton to MHWs and provide valuable insights into their ecological consequences in upwelling systems.

## Results

### MHWs in the CCE region

In the past 30 years (1993–2022), intense MHWs were predominantly concentrated along the coastal CCE region that contains the highest phytoplankton biomass (Fig. 1a), particularly around Point Conception, where the averaged MHWs intensity exceeds 2.3 °C. Correspondingly, this region experiences severe declines in surface CHL (Supplementary Fig. 1, 2). To characterize the temporal evolution of these events, we further examined the monthly mean MHWs intensity and spatial coverage of the study area (blue box in Fig. 1a), as a function of time. The results (Fig. 2a) indicate that the most severe and frequent events occurred during positive Pacific Decadal Oscillation (PDO) years (Fig. 2b), which are typically associated with suppressed coastal upwelling and increased net downward surface heat flux<sup>45</sup>. Here, a given month is labeled as “MHW month” if more than 50% of the study area experiences MHW conditions and the regional mean intensity exceeds 1 °C. Based on this definition, a total of 68 MHW months were identified between 1993 and 2022. Among these, 23 CalCOFI cruises (\* in Fig. 2) were conducted under MHWs in CCE, providing valuable in situ observations to assess ecosystem responses to extreme warming.

### Vertical CHL responds to MHWs

Based on 687 sections derived from 6 CalCOFI cruise lines collected between 1993 and 2022, we computed CHL anomalies ( $N = 35,754$ ) within the 200-m depth water column during MHWs (filled circles with asterisks in Fig. 2) to examine the vertical response of CHL to these extreme events (Fig. 3a). Intriguingly, we observed an unexpected vertical structure in the CHL pattern, characterized by negative anomalies in the surface layer accompanied by positive anomalies at depth, which has rarely been captured in this region by previous studies relying on satellite observations or vertically integrated investigations. In order to better quantify this phenomenon, we further assessed the vertical distribution of CHL anomalies at each depth level within the CalCOFI region (Fig. 3b). The results reveal a significantly reduction in CHL (mean:  $0.08\text{--}0.15 \mu\text{g L}^{-1}$ ) from surface to 50 m depth, with a concurrent increase ( $0.01\text{--}0.05 \mu\text{g L}^{-1}$ ) below 70 m depth during MHWs. The maximum negative anomalies occur at depths of 20–40 m, while the most pronounced positive anomalies were located around 70–80 m depth. Although the magnitude of subsurface positive anomalies was much smaller at individual depths compared to surface negative anomalies, their cumulative effect remains substantial when vertically integrated ( $-2.85 \mu\text{g L}^{-1}$  at surface versus  $1.62 \mu\text{g L}^{-1}$  at subsurface, exceeding 50% of the surface reduction magnitude), presenting a non-negligible contribution when estimating variability of vertically integrated CHL. This vertical redistribution may help explain why no significant correlations were previously found between MHW intensity/duration and

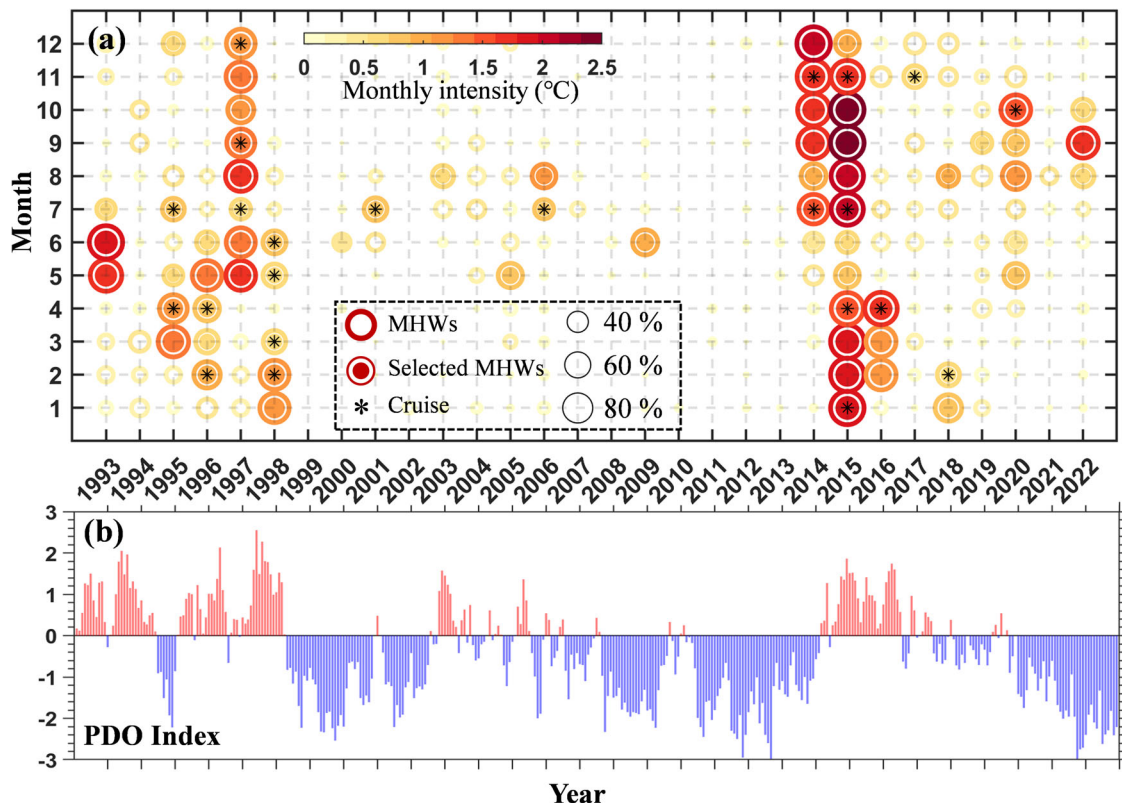


**Fig. 2 | MHWs occurrences and PDO index.** **(a)** MHW occurrences in the CalCOFI region based on OISST. A color and radius of unfilled circles represent the monthly mean intensity and spatial coverage (%) of MHWs, respectively. Filled circles indicate months when more than 50% area (Fig. 1) is under MHW conditions

and the regional mean intensity exceeds 1 °C, labeled as “MHW month”. Asterisks denote MHW months when CalCOFI cruises were conducted. **b** Pacific Decadal Oscillation (PDO) Index.

vertically integrated CHL<sup>46</sup>, despite surface CHL showing strong statistically significant correlations with MHWs. It may also elucidate the unexpected positive depth-integrated CHL anomaly during 2015–2016 El Niño in the CCS<sup>47</sup>.

Since this phenomenon was consistently observed across all CalCOFI transects, we selected Line 90.0 for detailed analysis due to its relatively higher sampling density and superior data quality (Fig. 1b; described in the Data and Methods) to better understand the vertical structure of the CHL anomalies. Composite anomalies of all variables shown in Figs. 4 and 5 were averaged over MHW months during which CalCOFI cruises were conducted (asterisks in Fig. 2).

Composite temperature anomalies across four seasons show that the most intense warming events happened during winter and fall<sup>41</sup>. Previous studies have demonstrated that vertical advection, which is associated with wind-driven reduced upwelling<sup>9,29,39,41,48–50</sup> and deepened thermocline<sup>32</sup>, constitutes the dominant driver of MHW development in the CCE. Thus, warming signals are observed in the subsurface across all four seasons, with particularly intensified warming at depth during winter due to weak stratification<sup>40,41</sup>. Figure 4e–h illustrates the seasonal distributions of CHL anomalies along Line 90.0, offering insight into phytoplankton responses to MHWs. This vertically decoupled variability was detected across all seasons, extending from onshore to offshore regions. The maximum reduction in CHL occurs around the SCML depth (red dashed lines in Fig. 4e–h), whereas CHL exhibited anomalous increases below the SCML during warming events. Due to the varying nutrient and physical environments between onshore and offshore, the SCML does not occur at a fixed depth but deepens as the offshore distance increases. Consequently, layers around 60-m depth (gray bar in Fig. 3b) contain positive anomalies onshore but negative anomalies offshore, resulting in no statistically significant change during MHWs when anomalies are depth-aggregated.

This finding highlights a decoupled vertical structure in CCE phytoplankton dynamics during MHWs, whereby subsurface phytoplankton biomass anomalies contradict the conventional paradigm of the reduced CHL pattern. The significant negative anomalies of surface CHL, which have been widely reported in the CCE, were mainly driven by reduced nutrient availability due to weakened upwelling<sup>29,36,51</sup>. However, the subsurface positive anomalies have rarely been documented, and the underlying mechanism remains unclear, challenging our understanding of MHW-induced ecological disturbances in the CCE. Therefore, the remainder of this study focuses on elucidating the mechanisms governing subsurface CHL enhancement during MHWs in this eastern boundary upwelling system.

#### Environmental anomalies during MHWs

Vertical variability in CHL is regulated by both hydrodynamic and biogeochemical processes<sup>44</sup>. Thus, we examined the variability of key environmental variables during MHWs along CalCOFI Line 90.0 (Fig. 5a–h) to explore the potential drivers of subsurface CHL anomalies. Composite temperature anomalies reveal that the most intense warming occurs 100–200 km offshore, extending from the surface to the ~100 m depth. In addition, salinity significantly increased in the upper 100 m layer, possibly due to the enhanced evaporation from warmer seawater or to weakened transport of fresher waters from the north. Below 100 m depth, salinity shows a negative anomaly at a similar distance (100–200 km from the coast), and its distribution indicates that the negative salinity anomaly originates from deeper layers. According to the abovementioned mechanism of the MHWs in this region as well as the distribution of warming signal, these salinity anomalies indicate a reduction in the upward transport of salt deep water—consistent with suppressed upwelling. Additionally, negative salinity anomalies near the offshore boundary of the transect imply that lateral

**Fig. 3 | Vertical responses of CHL to MHWs.** **a** Scatter density plot of CHL anomalies during MHWs, derived from vertical profiles at all stations across six CalCOFI lines. **b** Boxplot of CHL anomalies at 10-m depth intervals. The vertical dashed line indicates zero anomaly, and red lines denote the median. Green boxes indicate depths where anomalies are statistically different from zero (T-test;  $p < 0.05$ ). Vertically integrated CHL anomalies were calculated separately for the surface layer (from surface to SCML depth) and the subsurface layer (SCML depth to 200 m) at each station, and then averaged across all stations within the CalCOFI region.

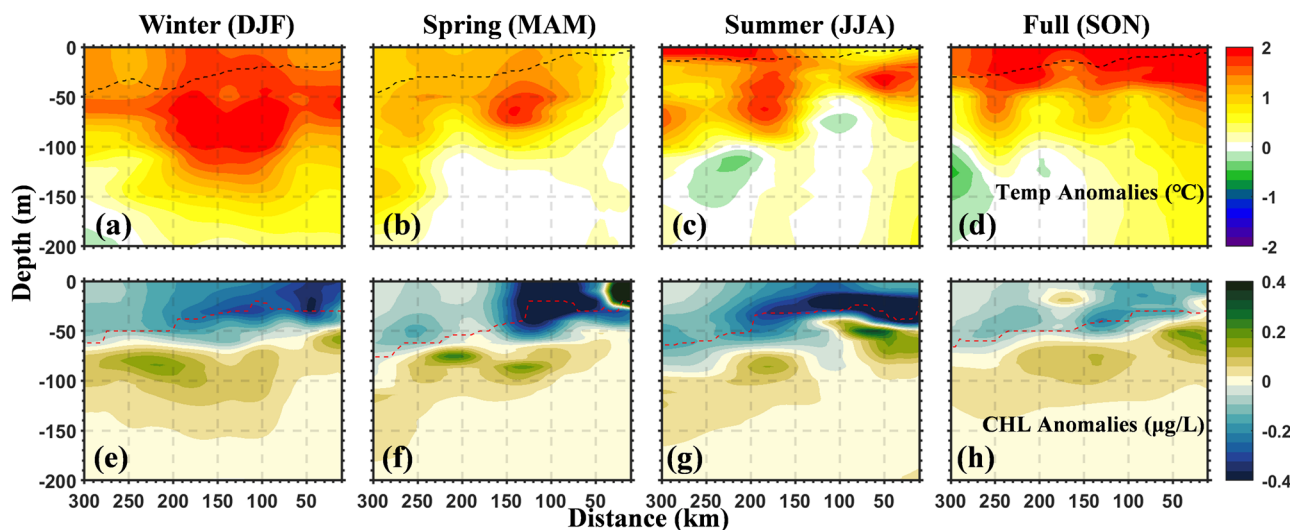
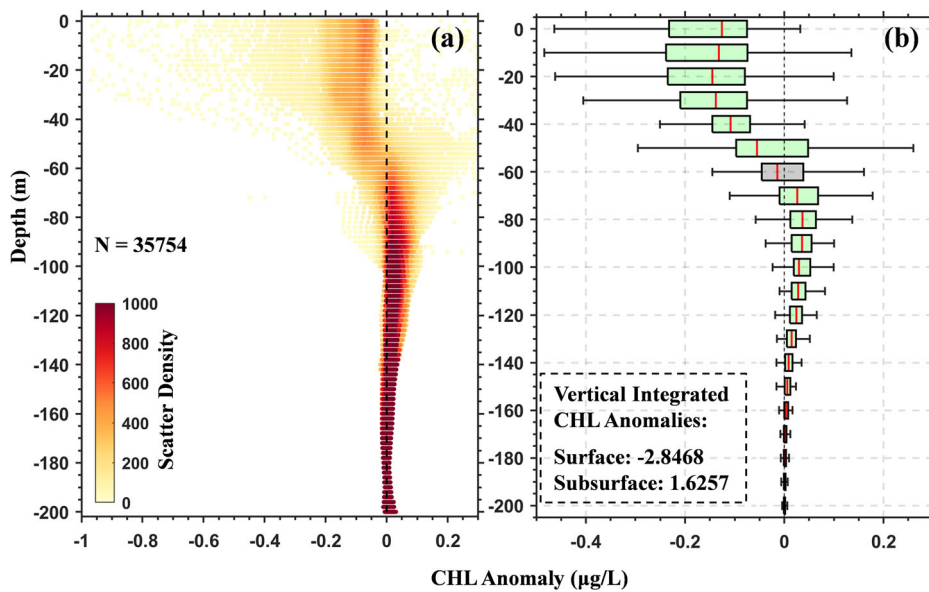


**Fig. 4 | Seasonal patterns of vertical CHL and temperature anomalies.** Seasonal anomalies of temperature (a–d) and CHL (e–h) during MHWs along CalCOFI Line 90.0 (DJF, MAM, JJA, SON represent winter: December–February, spring: March–May, summer: June–August, and fall: September–November, respectively).

Black and red dashed lines denote the mixed layer and the subsurface chlorophyll maximum layer (SCML) depth, respectively. Anomalies were calculated based on data from MHW months during which CalCOFI cruises were conducted (asterisks in Fig. 2).

intrusions may also contribute to the observed freshening, as projections under future warming scenarios have indicated<sup>52</sup>.

For the nutrient environment, as expected, phosphate and nitrate show consistent declining patterns along their respective isolines throughout the water column during MHWs, with the strongest reductions occurring between 50 and 100 m depth, coinciding with the depths of maximum CHL positive anomalies. Along the cross-shore direction, nutrient depletion was most pronounced between 100 and 200 km from the coast, where suppressed upwelling occurred. These nutrient patterns likely reflect a combined effect of weakened upwelling and enhanced consumption by increased subsurface phytoplankton biomass. Positive oxygen anomalies exhibited a similar subsurface pattern with the nutrients, further supporting the interpretation that observed nutrient reductions are driven by both physical and biogeochemical processes. Notably, other biogeochemical processes, such as the remineralization and grazing, may also contribute to the patterns of CHL, oxygen, and nutrients during MHWs. However, in this study, we mainly focus on the possible variations driven by the growth and mortality of the phytoplankton.

Overall, compared with climatological conditions, the SCML deepened by approximately 8 m (Fig. 5g), and the average nitracline depth (defined as the depth where nitrate concentration first exceeds  $1 \mu\text{mol L}^{-1}$ ) also deepened from 21 to 33 m depth during MHWs. Such shifts are consistent with prior findings in this region<sup>46,51</sup>. Moreover, this decoupled pattern becomes more pronounced as MHW intensity increases (Supplementary Fig. 3), with the magnitude of the subsurface anomalies increasing accordingly.

To further support our descriptions of local physical and biogeochemical variability, we incorporated output from CMEMS BGC and PHY numerical models. Prior to utilizing BGC-derived variables, we conducted comprehensive validation against satellite and in-situ observations (see Supplementary Note. 1). In general, the model demonstrates satisfactory performance in simulating CHL dynamics within the study region (Supplementary Fig. 4, 5) and, critically, it successfully reproduces the vertically decoupled CHL structure and associated nutrient-oxygen patterns observed during MHWs (Supplementary Fig. 6), showing good agreement with the CalCOFI data (Fig. 5). Outputs from the PHY model were not further validated, as its skill has been well established in this region<sup>31,53,54</sup>.

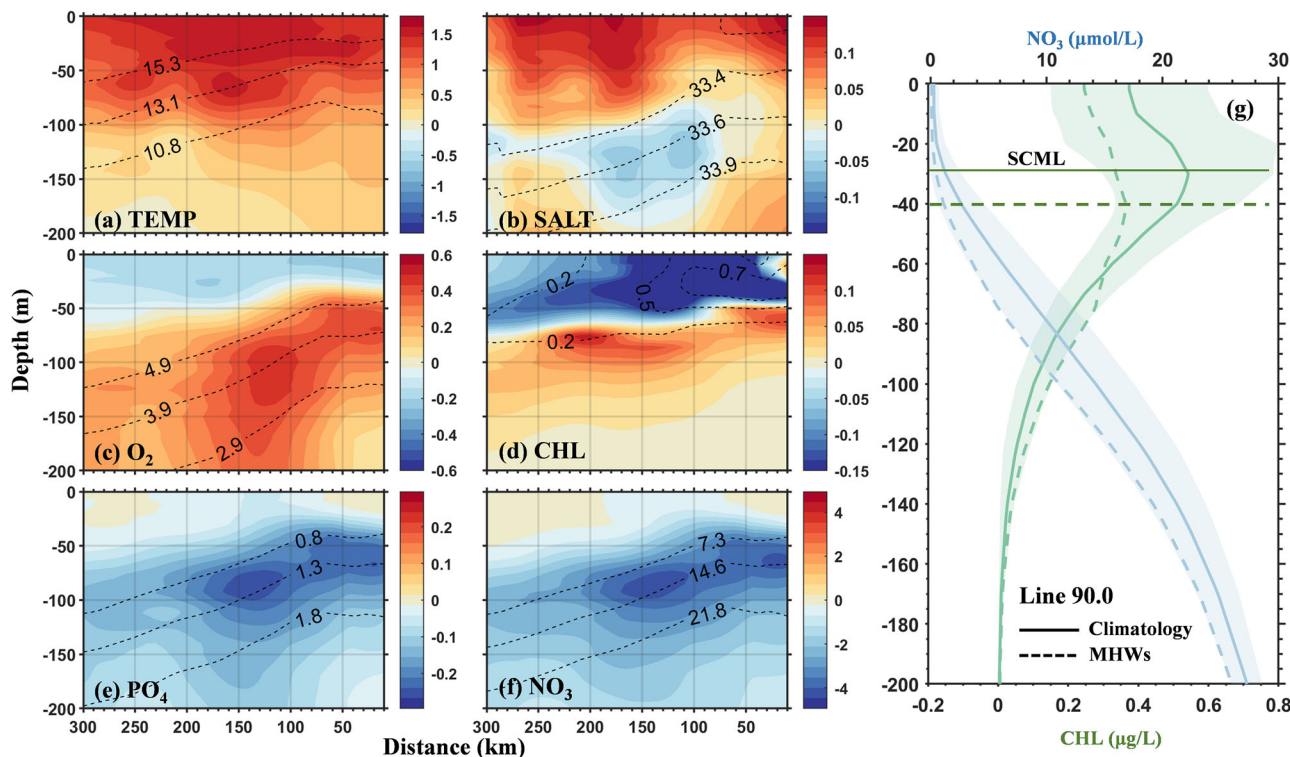


**Fig. 5 | Composite anomalies of environmental variables during MHWs.** a–f Composite anomalies of temperature (TEMP; °C), salinity (SALT; PSU), dissolved oxygen ( $O_2$ ; ml L<sup>-1</sup>), CHL ( $\mu\text{g L}^{-1}$ ), phosphate ( $PO_4$ ;  $\mu\text{mol L}^{-1}$ ), and nitrate ( $NO_3$ ;  $\mu\text{mol L}^{-1}$ ) during MHWs, with contours representing climatological values.

g Vertical profiles of CHL (green), SCML (dark green), and nitrate concentration (blue) under climatology (solid lines) and MHWs (dashed lines) states, averaged along the offshore distance of CalCOFI Line 90.0.

Vertical profiles of simulated physical variables clearly reproduce the key dynamic processes described above (Fig. 6). Maximum salinity anomalies occurring 100–200 km offshore below 100 m depth exhibit clearer extension both towards the depth and further offshore (Fig. 6e). A significant upwelling zone indeed exists within this offshore band, with its intensity significantly reduced during MHWs (Fig. 6f). Additionally, enhanced eastward advection was also observed offshore, potentially transporting fresher waters toward the upwelling region. Notably, anomalies in Fig. 6 were computed as the deviations from monthly climatology (whereas those in Fig. 5 are based on seasonal climatology derived from observations).

## Discussion

The subsurface environmental conditions described above explain the mechanisms driving the observed positive CHL anomalies. While the composite patterns in nutrients and oxygen anomalies likely result from weakened upwelling combined with enhanced phytoplankton activity, they do not directly account for the positive anomalies in subsurface phytoplankton biomass. To better understand the drivers of enhanced subsurface CHL during MHWs, it is necessary to further investigate the event-scale dynamics shaping this response. We therefore focused on the representative 2014–2015 MHW in the CCE to investigate the key mechanisms underlying this vertical structure.

Unlike the large-scale North Pacific warming event (“the Blob”), the 2014–2015 MHW along the California Coast is primarily driven by intermittent air-sea heat flux, horizontal and vertical heat advection anomalies<sup>33,55</sup>. Specifically, MHW in 2014 was driven by both anomalous vertical heat advection and air-sea heat flux<sup>55</sup>, whereas in 2015, alongshore heat advection (increased poleward volume transport and warmer-than-average temperature of the California Undercurrent) also contributed to the anomalous warming, in addition to the aforementioned drivers<sup>33</sup>. In addition, both years featured notable positive cross-shore heat advection

anomalies<sup>33</sup>. With the primary physical drivers of the 2014–2015 MHW established, we next investigate the vertical CHL dynamics and associated environmental parameters within the CalCOFI region (Fig. 7). Anomalies are calculated as deviations from monthly climatology (averaged over the CalCOFI region), with long-term signals (more than 5 years) removed using a high-pass Butterworth filter.

Model simulations revealed that positive subsurface CHL anomalies initially occurred around 50 m depth and progressively deepened to ~150 m as the MHW developed (Fig. 7a). More specifically, the seasonal chlorophyll bloom that typically originates in April 2014 and persists through August in climatology, was suppressed before July due to MHW disruption (solid and dashed black contours in Fig. 7d). Concurrently, phytoplankton exhibited deeper and more pronounced subsurface growth (solid and dashed white lines in Fig. 7d), contributing to the positive anomaly. This anomaly attenuated with the seasonal shoaling of the SCML around November (black lines in Fig. 8a). During a subsequent proliferation phase in January 2015 (Supplementary Fig. 7), surface productivity was again suppressed under stronger MHW conditions (Supplementary Fig. 8), with enhanced growth occurring below 50 m depth.

Our analysis of environmental variable anomalies in the CCE, integrated with established theoretical frameworks of phytoplankton dynamics<sup>24,36,44,51,56</sup>, suggests that nutrient dynamics is a primary driver governing vertical CHL variability. However, the phytoplankton biomass would be expected to decline rather than show positive anomalies as the SCML deepens due to reduced nutrient availability in deep waters<sup>57</sup>. In such cases, light availability may become another dominant factor, especially when phytoplankton grow below the climatological euphotic depth. In a highly productive coastal system like CCE, underwater light conditions depend not only on surface irradiance but also on vertical light penetration, which is strongly influenced by water turbidity and the phytoplankton self-shading effect<sup>58,59</sup>. Thus, we quantified the Photosynthetically Active Radiation (PAR), and nitrate flux across the five boundaries of the CalCOFI

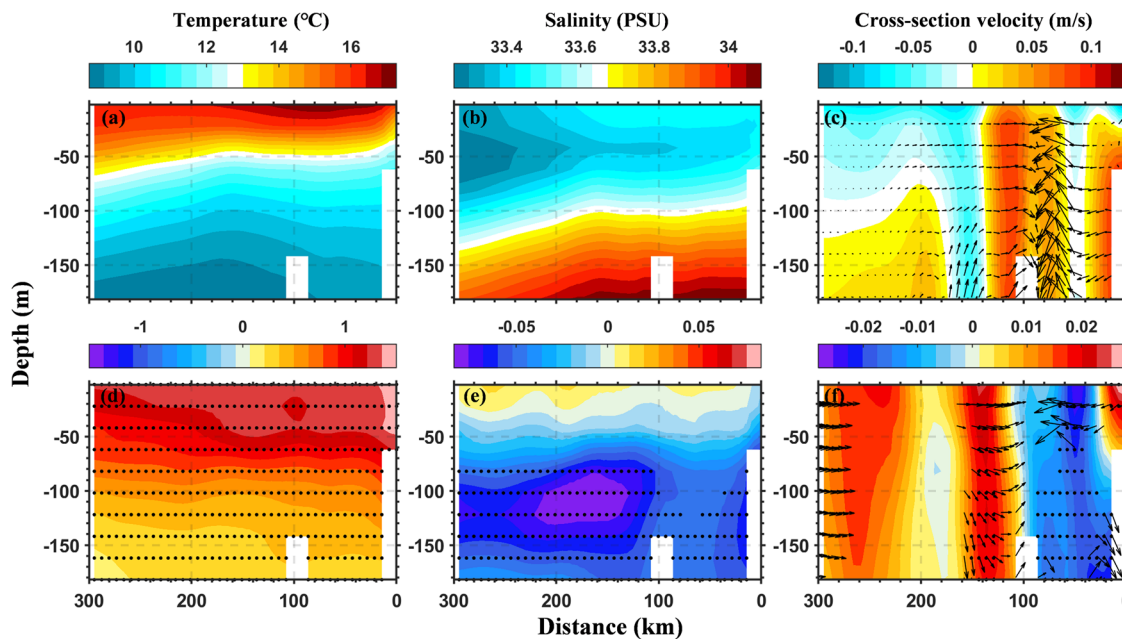


**Fig. 6 | Physical conditions during MHWs.** Climatological (a–c) profiles of temperature, salinity, and cross section velocity and their composite anomalies (d–f) during MHWs along CalCOFI Line 90.0. Black dots denote the anomalies are significantly different from zero (T-test;  $p < 0.05$ ). Arrows in (c) and (f) represent the

mean along-section and vertical velocities and their anomalies (only shown when anomalies in both directions are significantly different from zero), the vertical component of velocity is multiplied by 1000 for better visualization. Note that the composite anomalies are calculated by the same MHW month as Fig. 5.

region (Fig. 7f) to further assess the contributions of light availability and nutrient supply to the subsurface CHL during MHWs. Surface PAR data were obtained from the MODIS PAR product, while subsurface PAR was calculated using the same three-waveband light penetration scheme as the CMEMS-BGC model. Advection and diffusion are the major physical processes that control the nitrate flux in the water column. In an upwelling system like the CCE, the contribution of diffusion is generally considered minor compared to advection<sup>60,61</sup>. Thus, we mainly focus on the advection term in this study.

Positive nitrate anomalies were observed between 50 and 100 m depth prior to the onset of both MHWs in June 2014 and 2015 (Fig. 7c), potentially creating a more favorable nutrient environment for phytoplankton growth here. Nitrate flux calculations revealed positive anomalies across all three spatial dimensions (cross-shore: westward; alongshore: northward + southward; vertical: upward + downward) in June 2014, and the positive vertical flux resulted from both enhanced import through the bottom boundary and reduced export through the upper boundary. In June 2015, elevated nitrate input occurred primarily through vertical and cross-shore transport (Fig. 7f). Subsequently, nitrate anomalies for both events diminished as the MHW progressed, with vertical and alongshore nitrate flux anomalies turning negative. Positive cross-shore nitrate fluxes were observed during nearly all events between 2014 and 2015, closely aligning with net heat advection in the same direction<sup>33</sup>.

Regarding the light conditions, significantly positive PAR anomalies were observed at 50 m depth throughout the 2014–2015 events, while sustained surface PAR enhancement occurred during the latter event (July to December 2015). Compared to the surface, subsurface PAR showed stronger correspondence with the vertical distribution of positive CHL anomalies, which exhibited progressive deepening in response to two distinct phases of subsurface PAR enhancement (June–October 2014 and January–September 2015). These results indicate that, although the subsurface light condition can be directly influenced by the surface irradiance, phytoplankton productivity at depth is more sensitive to light availability within these specific layers, and the self-shading effect of the phytoplankton can significantly alter the light penetration throughout the water column during MHWs. While the depth of the positive CHL anomalies aligned well with the PAR anomalies at 50-m depth, light availability alone cannot fully

explain the observed subsurface phytoplankton activity. For example, the positive subsurface CHL anomaly reached its maximum intensity at 60 m depth in May 2015, despite the absence of significant subsurface PAR enhancement. In this case, enhanced productivity was primarily supported by positive nitrate anomalies transported via upwelling and cross-shore advection. Specifically, when along-shore and vertical nitrate flux anomalies were negative in June and July 2015, nitrate anomalies still remained positive due to cross-shore nitrate flux supply, suggesting the non-negligible contribution of lateral nutrient supply during warming events.

These findings suggest that light condition variations induced by atmospheric processes and phytoplankton self-shading effects might influence both the depth and intensity of subsurface phytoplankton growth during MHWs. However, vertical and cross-shore nitrate fluxes act as critical additional drivers sustaining subsurface productivity under these anomalous conditions.

Building upon the detailed examination of specific 2014–2015 MHW events in the CCE, we further investigated the background states of these potential controlling factors during all MHWs from 1993 to 2022. Mean net nitrate flux anomalies across the five boundaries during MHWs are shown in Table 1. Compared to climatological conditions, a significant net influx of nitrate was observed from the western boundary during MHWs ( $1.90 \text{ kmol s}^{-1}$ ;  $P < 0.01$ ), while no significant anomalies were found at the northern or southern boundaries. Vertically, less nitrate ( $-1.02 \text{ kmol s}^{-1}$ ;  $P < 0.01$ ) was upwelled into subsurface water through the bottom boundary and reduced nitrate ( $-0.38 \text{ kmol s}^{-1}$ ;  $P < 0.01$ ) was exported through the top boundary, reflecting to the suppressed upwelling during MHWs. These results suggest that, although vertical nutrient supply was substantially weakened, increased lateral input from the western boundary partially offsets the overall nutrient deficit. It can be anticipated that without this supplementary input, local nutrient levels and thus phytoplankton productivity, would likely have declined even further. This finding aligns with previous projections based on climate models, which suggest that climate-driven increases in nutrient-rich water transport through the western boundary could enhance productivity in the CCE under future warming scenarios<sup>52</sup>. Our results, derived from observed extreme warming events, support this type of local mechanism and underscore the pivotal role of lateral nutrient transport in sustaining ecosystem productivity under MHW conditions.

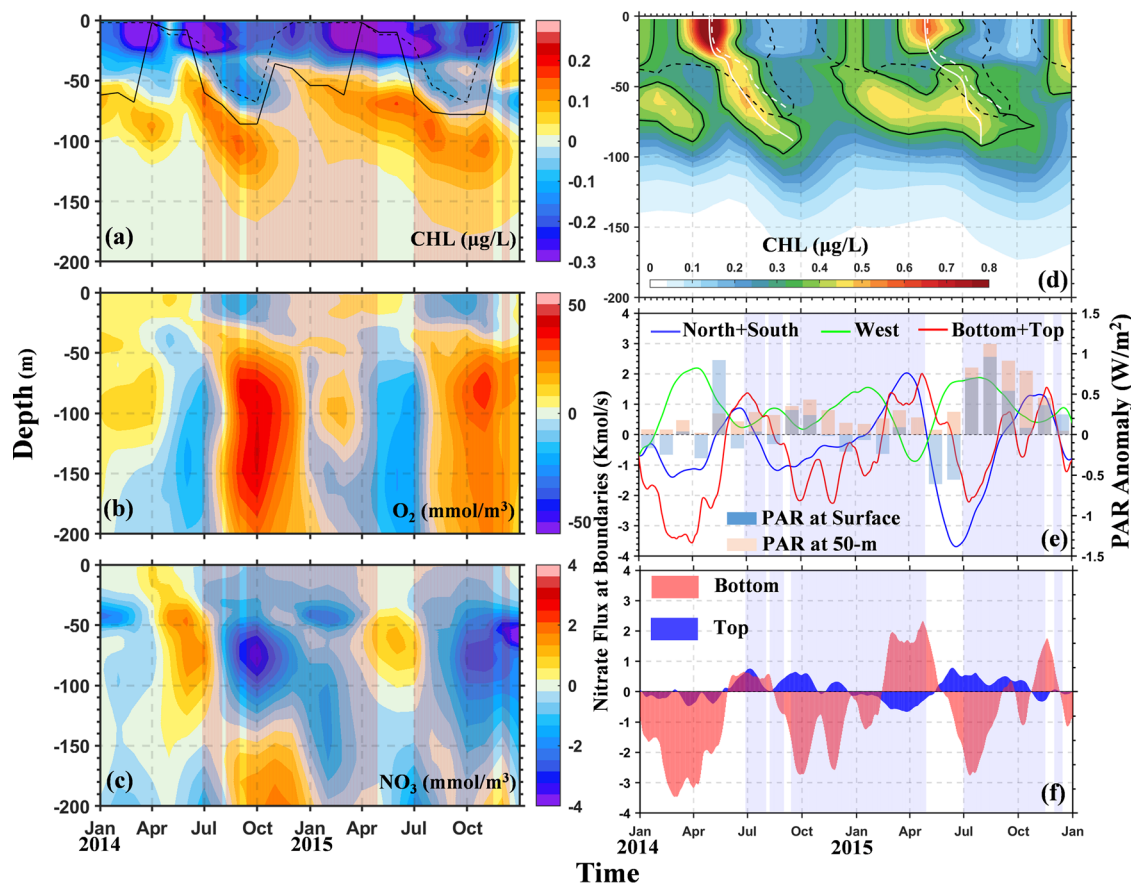


**Fig. 7 | Temporal evolutions of local biogeochemical environments and nitrate flux.** a–c Vertical anomalies of simulated CHL, dissolved oxygen, and nitrate, averaged over the CalCOFI region, shown as a function of time. Dashed and solid lines in (a) refer to the climatological and real SCML depth, respectively. d Modeled vertical CHL distribution from 2014 to 2015. Dashed and solid contours (white lines) represent the climatological and real  $0.4 \mu\text{g L}^{-1}$  CHL isoline (SCML),

respectively. PAR at surface is divided by 5 for visualization. e Nitrate flux anomalies across the five boundaries of the CalCOFI region: alongshore (blue), cross-shore (green), and vertical (red), with positive values indicating inward transport. Blue and red bars denote anomalies of PAR at the surface and 50-m depth, respectively. f Nitrate flux anomalies across the bottom and top boundaries.

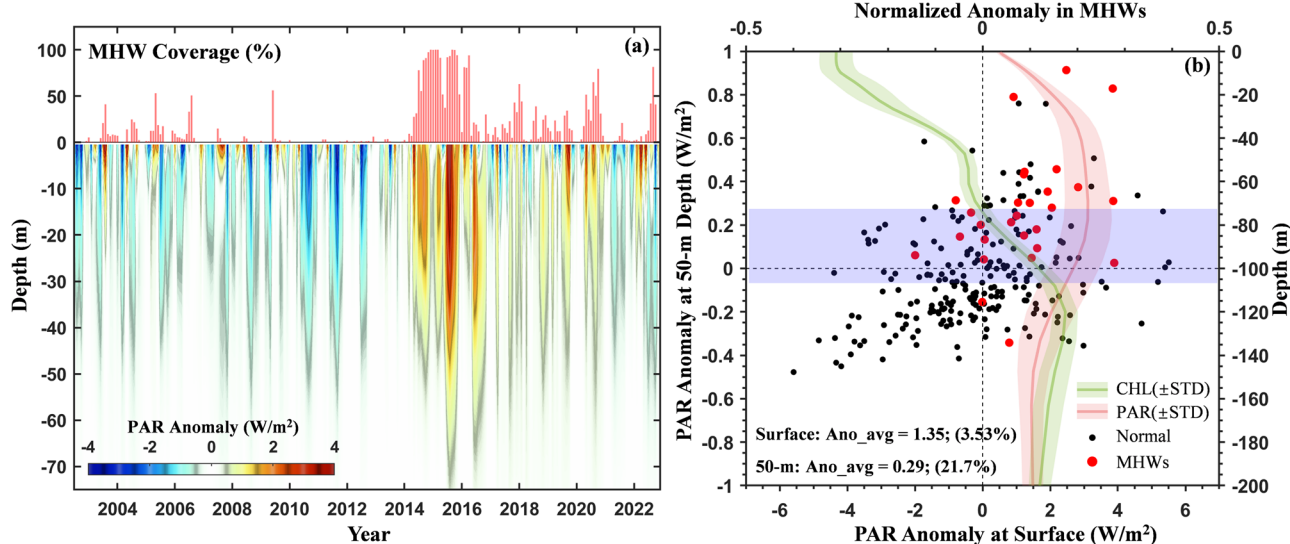


**Fig. 8 | Light availability during MHWs.** a Timeseries of vertical light conditions. Red bars represent the monthly coverage of the MHW area (%). Shading denotes the PAR anomalies at different depths. b Black (red) dots represent the monthly PAR at

the surface and at 50-m depth under normal (MHW) conditions. The green and red lines refer to normalized anomalies of CHL and PAR under MHWs. All values here are regionally averaged over the CalCOFI region.

**Table. 1 | Net nitrate flux anomalies**

Boundary	South	North	West	Bottom	Top
Net Nitrate Flux Anomalies	1.81	-0.83	1.90	-1.02	0.38
P-value	0.11	0.40	<0.01	<0.01	<0.01

Net nitrate flux anomalies (unit: kmol/s) at five boundaries and their p-values (T-test), directions into the CCE region are positive

Moreover, light condition in the subsurface layers showed varying degrees of enhancement under MHWs (Fig. 8a), particularly during 2014–2016 MHW, the average PAR increment throughout the water column exceeded  $4\text{ W m}^{-2}$ . In order to further examine whether this light enhancement results from increased surface irradiance influenced by atmospheric processes, or reduced self-shading effect of the suppressed surface phytoplankton biomass, we examined PAR at two layers for every event. As shown in Fig. 8b, most MHW months exhibited positive PAR anomalies at 50 m depth, with only two exceptions showing negative values. Surface PAR also increased in the majority of events. On average, surface PAR in the CalCOFI region increased by 3.53% ( $p < 0.01$ ; T-test), likely due to reduced cloud cover and enhanced incoming solar radiation<sup>62</sup>. However, the reduction of the surface phytoplankton significantly enhanced the light penetration in the water column, causing the subsurface PAR to significantly increase by 21.7%, which provides better light availability for the phytoplankton growth at depth. Further support for this mechanism comes from the co-location of normalized CHL and PAR anomalies during MHWs. Specifically, positive CHL anomalies emerged at depths where normalized PAR anomalies reached their maximum (shaded purple area in Fig. 8b), highlighting the tight coupling between subsurface light availability and phytoplankton growth.

Thus, the mechanisms underlying the vertical structure of CHL response to MHWs in the CCE become evident. Suppressed upwelling limits the nutrient delivery to surface waters, leading to a marked decline in surface CHL. Simultaneously, enhanced lateral advection of nutrient-rich waters through the western boundary provides an additional nutrient source to the subsurface layers. Improved light penetration driven by decreased surface phytoplankton biomass, combined with increased surface irradiance, further enhances light availability in subsurface waters. The co-occurrence of lateral nutrient supply and improved light conditions promotes phytoplankton growth at depth, ultimately driving the anomalous enhancement of subsurface CHL during MHWs in the CCE.

However, despite the supplementary lateral input, composite nutrient anomalies during MHWs remain negative, suggesting that lateral nutrient import may not fully compensate for the reduced vertical supply. Additionally, under low-light conditions, the efficiency of nutrient utilization decreases<sup>63</sup>, meaning that intensified phytoplankton productivity at depth consumes greater amounts of available nutrients, further exacerbating local nutrient depletion.

The vertical heterogeneity in CHL responses to climate change and extreme events has attracted increasing attention very recently. For example, in the open Arctic Ocean, diatom blooms have been observed near the seafloor rather than at the surface, owing to improved light conditions at depth<sup>64</sup>. In the Sargasso Sea, subsurface phytoplankton biomass became increasingly decoupled from the surface community under long-term warming and enhanced stratification, leading to pronounced subsurface CHL enrichment despite surface depletion, with total phytoplankton carbon showing an overall increase over the past decade<sup>43</sup>. Similarly, phytoplankton biomass in the central tropical Indian Ocean exhibits contrasting seasonal variability between surface and subsurface layers<sup>65</sup>. Considering the projected increase in both intensity and frequency of MHWs on global scales and in the CCE region<sup>3,4,66</sup>, developing a comprehensive understanding of vertical CHL dynamics during MHWs is crucial for predicting ecosystem responses under future ocean climate scenarios.

## Conclusion

In this study, we integrated long-term CalCOFI cruise observations, satellite remote sensing data, and coupled physical-biogeochemical model products

to investigate the vertical CHL response to MHWs in the CCE. Our results revealed that the vertical response of CHL to MWHs is not uniformly decreased, but exhibits vertical structure with decreases in the surface layer and increases in the subsurface layer. This pattern is inherently challenging to detect through satellite-based observations. Consistent with previous studies, the reduction in surface CHL is primarily attributed to suppressed nutrient supply due to weakened upwelling. In contrast, the increase of subsurface CHL is linked to two key processes: (i) enhanced lateral nutrient transport through the western boundary, which provides additional nutrient supply under low-level nutrient conditions caused by reduced upwelling; (ii) improved light availability at depth, resulting from both increased surface irradiance and enhanced light penetration due to reduced surface phytoplankton biomass.

To date, satellite remote sensing remains the most effective way to monitor phytoplankton dynamics in various spatial scales. However, it is inherently limited to near-surface signals and may miss significant subsurface variability, where phytoplankton communities are often more abundant and more sensitive to environmental perturbations<sup>43</sup>. Our findings suggest that subsurface phytoplankton may play an important role in shaping the vertical CHL structure and its response to extreme climate events. These insights provide valuable perspectives for interpreting biogeochemical variability and assessing ecosystem responses across trophic levels under future ocean warming scenarios<sup>46,67</sup>.

Finally, we must acknowledge the limitations of this study, particularly our exclusion of biological processes such as zooplankton grazing and the physiological behavior of phytoplankton, which remain difficult to observe and simulate accurately. Further, enhanced in-situ observations, such as those carried out by the CCE-LTER in process cruises<sup>68</sup> and systematic sensitivity experiments using advanced coupled physical-ecological models in the CCE<sup>69–72</sup> are necessary for comprehensive quantification of the regulatory mechanisms governing these complex vertical CHL dynamics during MHWs.

## Data and Methods

### In situ sampling data

In situ observations were obtained from the bottle database collected during quarterly CalCOFI cruises, including 6 transect lines (93.3 to 76.7) in the CCE (Fig. 1a). Vertical profiles of seawater temperature, salinity, dissolved oxygen, chlorophyll-a concentration, and nutrients (phosphate, nitrite) from 1993 to 2022 were analyzed. The anomalies of these environmental variables during MHWs were computed as deviations from seasonal climatology for each transect.

Although CalCOFI generally conducts four cruises per year, sampling frequency has varied due to occasional cancellations or additions (e.g., monthly sampling along Line 90.0 in 1998). Among all lines, Line 90.0 recorded the highest number of valid transects (121; Fig. 1b).

To further evaluate the quality of observed CHL data, we first interpolated vertical chlorophyll-a profiles from each station onto a standardized 0–200 depth grid. Depths with valid data were marked as 1, and those without data were marked as 0. For each station, depths that contained valid data in at least three cruises were defined as climatologically valid layers. The quality of each profile was then calculated as the percentage of these valid layers that were successfully sampled during a given cruise. Results showed that Lines 80.0, 86.7, 90.0, and 93.3 had consistently high data quality, with Line 90.0 standing out due to both dense sampling and superior quality. Therefore, we selected Line 90.0 for detailed analysis.

### Satellite surface CHL data

Surface CHL data were derived from the Copernicus-GlobColour multi-sensor merged product (OCEANCOLOUR\_GLO\_BGC\_L4\_MY\_009\_104), integrating observations from SeaWiFS, MODIS, MERIS, OLCI, and VIIRS sensors. It provides daily 4-km resolution surface CHL from Aug 1997 to present, and has been widely employed both for global and regional CCE applications<sup>73,74</sup>.

## Physical and biogeochemical model outputs

To further investigate the dynamic mechanisms underlying this MHWs phenomenon, higher-resolution fields were required. Therefore, we incorporated model outputs from the Copernicus Marine Environment Monitoring Service (CMEMS) to assist our analysis. The physical reanalysis product (hereafter referred to as CMEMS-PHY) utilized here was derived from eddy-resolving GLORYS12V1 system (GLOBAL\_MULTIYEAR\_PHY\_001\_030), which provides data-assimilated global ocean fields at a horizontal resolution of  $1/12^\circ$  and 50 vertical levels, spanning from 1993 to two months prior to the present. This product has demonstrated improved fidelity in simulating physical processes in the CCE region<sup>53</sup>, and can therefore provide seawater temperature, salinity, and ocean currents for this study. The biogeochemical model outputs (CMEMS-BGC) are obtained from the Global Ocean Biogeochemistry Hindcast product (GLOBAL\_MULTIYEAR\_BGC\_001\_029), which is based on the PISCES model<sup>75</sup> and forced by the FREE-GLORYS2V4 ocean physical hindcast produced at Mercator-Ocean. Notably, no assimilation was applied to this BGC product. It provides daily chlorophyll-a, nitrate, phosphate, silicate, dissolved oxygen, and primary production on a uniform  $0.25^\circ$  horizontal grid with 75 standard levels, over the same temporal extent as the physical product. Prior to the analysis, variables from the physical products were interpolated onto the same spatial grid as the biogeochemical products to ensure consistency in data format.

## SST data and MHW identification

We adopted a widely used approach<sup>1</sup> to define MHW periods, which is when the Sea Surface Temperature (SST) exceeds the 90th percentile of the local climatology for at least 5 days, over the period 1993–2022. The SST data were obtained from the daily Optimum Interpolation Sea Surface Temperature (OISST) analysis product<sup>76</sup>, with a spatial resolution of  $0.25^\circ$  and spanning from 1920 to the present. Given that the rate of acclimatization or adaptation to warmer conditions is generally assumed to be lower than the current rate of ocean warming for most ecosystems<sup>2,44</sup>, we used the period from 1982 to 2022 as a fixed baseline for constructing the climatology. In the following discussion, a month is labeled as an “MHW month” if more than 50% of the study area (Fig. 1) is under MHW conditions and the regional mean intensity exceeds  $1^\circ\text{C}$ . Note that the long-term trend of SST from 1982–2022 has been removed before identification based on the recommendation of ref. 77.

## Nutrient supply and light availability

As nitrate is the main nutrient limiting primary production in the CCE<sup>52</sup>, we evaluated impacts of nutrient supply on CHL dynamics by quantifying net nitrate flux transported into the CalCOFI region through five boundaries, including three horizontal boundaries (south, north, west; blue box in Fig. 1a) and two vertical boundaries (bottom: 200 m depth; top: 50 m depth). Nitrate fluxes were estimated as the product of daily nitrate concentration (CMEMS-BGC) and velocity (CMEMS-PHY), integrated over the entire cross-sectional area. Notably, advective fluxes directed into the control volume are positive (i.e., poleward flow at the southern boundary, equatorward flow at the northern boundary, eastward flow at the western boundary, upwelling at the bottom boundary, and downwelling at the top boundary).

Light availability in this study is quantified using Photosynthetically Active Radiation (PAR). Monthly mean surface PAR from 2002 to 2022 was obtained from 4-km MODIS (Terra + Aqua; MCD18A2) PAR product, which applies a multi-temporal surface reflectance algorithm and a look-up table approach to estimate incident PAR<sup>78</sup>. Vertical PAR profiles were computed by the surface MODIS PAR, using the same three-waveband light penetration scheme<sup>79</sup> as the CMEMS-BGC model<sup>75</sup>, incorporating the effects of phytoplankton biomass and self-shading based on CHL profiles from the CMEMS-BGC output.

## Data availability

CalCOFI in-situ observations used in the study were obtained from <https://calcofi.org/data/oceanographic-data/bottle-database/>. SST data were

downloaded from National Centers for Environmental Information (<https://www.ncei.noaa.gov/products/optimum-interpolation-sst>). BGC and PHY model products were derived from Copernicus Marine Data Store (<https://data.marine.copernicus.eu/products>). MODIS surface PAR product was downloaded from <https://oceandata.sci.gsfc.nasa.gov/>.

## Code availability

Codes for the main results are available via Zenodo <https://zenodo.org/records/17098687>. Three-waveband light penetration scheme can be found through <https://forge.nemo-ocean.eu/nemo/nemo/-/tree/main/src/OCE/TRA>.

Received: 28 April 2025; Accepted: 25 September 2025;

Published online: 20 November 2025

## References

1. Hobday, A. J. et al. A hierarchical approach to defining marine heatwaves. *Prog. Oceanogr.* **141**, 227–238 (2016).
2. Oliver, E. C. et al. Marine heatwaves. *Annu. Rev. Mar. Sci.* **13**, 313–342 (2021).
3. Frölicher, T. L., Fischer, E. M. & Gruber, N. Marine heatwaves under global warming. *Nature* **560**, 360–364 (2018).
4. Oliver, E. C. et al. Longer and more frequent marine heatwaves over the past century. *Nat. Commun.* **9**, 1324 (2018).
5. Eakin, C. M., Sweatman, H. P. & Brainard, R. E. The 2014–2017 global-scale coral bleaching event: insights and impacts. *Coral Reefs* **38**, 539–545 (2019).
6. Smith, K. E. et al. Biological impacts of marine heatwaves. *Annu. Rev. Mar. Sci.* **15**, 119–145 (2023).
7. Wernberg, T. et al. An extreme climatic event alters marine ecosystem structure in a global biodiversity hotspot. *Nat. Clim. Change* **3**, 78–82 (2013).
8. Smale, D. A. et al. Marine heatwaves threaten global biodiversity and the provision of ecosystem services. *Nat. Clim. Change* **9**, 306–312 (2019).
9. Capotondi, A. et al. A global overview of marine heatwaves in a changing climate. *Commun. Earth Environ.* **5**, 701 (2024).
10. Gruber, N., Boyd, P. W., Frölicher, T. L. & Vogt, M. Biogeochemical extremes and compound events in the ocean. *Nature* **600**, 395–407 (2021).
11. Le Grix, N., Burger, F. A. & Frölicher, T. L. Surface and subsurface compound marine heatwave and biogeochemical extremes under Climate change. *Glob. Biogeochem. Cycles* **39**, e2025GB008514 (2025).
12. Hauri, C. et al. More than marine heatwaves: a new regime of heat, acidity, and low oxygen compound extreme events in the Gulf of Alaska. *AGU Adv.* **5**, e2023AV001039 (2024).
13. Wong, J., Münnich, M. & Gruber, N. Column-compound extremes in the global ocean. *AGU Adv.* **5**, e2023AV001059 (2024).
14. Smith, K. E. et al. Socioeconomic impacts of marine heatwaves: Global issues and opportunities. *Science* **374**, eabj3593 (2021).
15. Holbrook, N. J. et al. A global assessment of marine heatwaves and their drivers. *Nat. Commun.* **10**, 2624 (2019).
16. Frölicher, T. L. & Laufkötter, C. Emerging risks from marine heat waves. *Nat. Commun.* **9**, 650 (2018).
17. Marañón, E. Cell size as a key determinant of phytoplankton metabolism and community structure. *Annu. Rev. Mar. Sci.* **7**, 241–264 (2015).
18. Falkowski, P. G., Fenchel, T. & Delong, E. F. The microbial engines that drive Earth's biogeochemical cycles. *science* **320**, 1034–1039 (2008).
19. Thomas, M. K., Kremer, C. T., Klausmeier, C. A. & Litchman, E. A global pattern of thermal adaptation in marine phytoplankton. *Science* **338**, 1085–1088 (2012).
20. Barton, A. D., Irwin, A. J., Finkel, Z. V. & Stock, C. A. Anthropogenic climate change drives shift and shuffle in North Atlantic phytoplankton communities. *Proc. Natl. Acad. Sci.* **113**, 2964–2969 (2016).

21. Fernández-González, C. et al. Phytoplankton responses to changing temperature and nutrient availability are consistent across the tropical and subtropical Atlantic. *Commun. Biol.* **5**, 1035 (2022).
22. Le et al. Compound high temperature and low chlorophyll extremes in the ocean over the satellite period. *Biogeosci. Discuss.* **2020**, 1–26 (2020).
23. Noh, K. M., Lim, H.-G. & Kug, J.-S. Global chlorophyll responses to marine heatwaves in satellite ocean color. *Environ. Res. Lett.* **17**, 064034 (2022).
24. Zhan, W., Zhang, Y., He, Q. & Zhan, H. Shifting responses of phytoplankton to atmospheric and oceanic forcing in a prolonged marine heatwave. *Limnol. Oceanogr.* **68**, 1821–1834 (2023).
25. Hayashida, H., Matear, R. J. & Strutton, P. G. Background nutrient concentration determines phytoplankton bloom response to marine heatwaves. *Glob. Change Biol.* **26**, 4800–4811 (2020).
26. Peña, M. A., Nemcek, N. & Robert, M. Phytoplankton responses to the 2014–2016 warming anomaly in the northeast subarctic Pacific Ocean. *Limnol. Oceanogr.* **64**, 515–525 (2019).
27. Delgadillo-Hinojosa, F. et al. Impacts of the 2014–2015 warm-water anomalies on nutrients, chlorophyll-a and hydrographic conditions in the coastal zone of northern Baja California. *J. Geophys. Res.: Oceans* **125**, e2020JC016473 (2020).
28. Wyatt, A. M., Resplandy, L. & Marchetti, A. Ecosystem impacts of marine heat waves in the northeast Pacific. *Biogeosciences* **19**, 5689–5705 (2022).
29. Zhan, W. et al. Reduced and smaller phytoplankton during marine heatwaves in eastern boundary upwelling systems. *Commun. Earth Environ.* **5**, 629 (2024).
30. Di Lorenzo, E. & Mantua, N. Multi-year persistence of the 2014/15 North Pacific marine heatwave. *Nat. Clim. Change* **6**, 1042–1047 (2016).
31. Amaya, D. J., Miller, A. J., Xie, S.-P. & Kosaka, Y. Physical drivers of the summer 2019 North Pacific marine heatwave. *Nat. Commun.* **11**, 1903 (2020).
32. Wei, X., Li, K. Y., Kilpatrick, T., Wang, M. & Xie, S. P. Large-scale conditions for the record-setting Southern California marine heatwave of August 2018. *Geophys. Res. Lett.* **48**, e2020GL091803 (2021).
33. Zaba, K. D., Rudnick, D. L., Cornuelle, B. D., Gopalakrishnan, G. & Mazloff, M. R. Volume and heat budgets in the coastal California current system: Means, annual cycles, and interannual anomalies of 2014–16. *J. Phys. Oceanogr.* **50**, 1435–1453 (2020).
34. Cavole, L. M. et al. Biological impacts of the 2013–2015 warm-water anomaly in the Northeast Pacific: winners, losers, and the future. *Oceanography* **29**, 273–285 (2016).
35. Closset, I. et al. Diatom response to alterations in upwelling and nutrient dynamics associated with climate forcing in the California Current System. *Limnol. Oceanogr.* **66**, 1578–1593 (2021).
36. Landry, M. R. et al. Phytoplankton growth and grazing dynamics during anomalous heat wave and suppressed upwelling conditions in the southern California Current. *Deep Sea Res. Part I: Oceanogr. Res. Pap.* **210**, 104353 (2024).
37. McCabe, R. M. et al. An unprecedented coastwide toxic algal bloom linked to anomalous ocean conditions. *Geophys. Res. Lett.* **43**, 10,366–310,376 (2016).
38. Fischer A. D. et al. Nutrient limitation dampens the response of a harmful algae to a marine heatwave in an upwelling system. *Limnol. Oceanogr.*, (2024).
39. Zhang, Y., Du, Y., Feng, M. & Hobday, A. J. Vertical structures of marine heatwaves. *Nat. Commun.* **14**, 6483 (2023).
40. Köhn, E. E., Vogt, M., Münnich, M. & Gruber, N. On the vertical structure and propagation of marine heatwaves in the Eastern Pacific. *J. Geophys. Res.: Oceans* **129**, e2023JC020063 (2024).
41. Plume, G. et al. Vertical structure of subsurface marine heatwaves in a shallow nearshore upwelling system. *Sci. Rep.* **15**, 6353 (2025).
42. Yuan, T. et al. Vertical structures of marine heatwaves in the South China Sea: Characteristics, drivers and impacts on chlorophyll concentration. *J. Geophys. Res.: Oceans* **129**, e2024JC021091 (2024).
43. Viljoen, J. J., Sun, X. & Brewin, R. J. Climate variability shifts the vertical structure of phytoplankton in the Sargasso Sea. *Nat. Clim. Change* **14**, 1292–1298 (2024).
44. Cullen, J. J. Subsurface chlorophyll maximum layers: enduring enigma or mystery solved?. *Annu. Rev. Mar. Sci.* **7**, 207–239 (2015).
45. Ren, X., Liu, W., Capotondi, A., Amaya, D. J. & Holbrook, N. J. The Pacific Decadal Oscillation modulated marine heatwaves in the Northeast Pacific during past decades. *Commun. Earth Environ.* **4**, 218 (2023).
46. Chen, T. C. et al. Multi-Trophic Level Responses to Marine Heatwave Disturbances in the California Current Ecosystem. *Ecol. Lett.* **27**, e14502 (2024).
47. McClatchie S. et al. State of the California current 2015–16: comparisons with the 1997–98 El Niño. (2016).
48. Fewings, M. R. & Brown, K. S. Regional structure in the marine heat wave of summer 2015 off the western United States. *Front. Mar. Sci.* **6**, 564 (2019).
49. Datsin, M., Walter, R. K. & Mazzini, P. L. Effects of basin-scale climate modes and upwelling on nearshore marine heatwaves and cold spells in the California Current. *Sci. Rep.* **13**, 12389 (2023).
50. Cervantes, B. T., Fewings, M. R. & Risien, C. M. Subsurface temperature anomalies off Central Oregon during 2014–2021. *J. Geophys. Res.: Oceans* **129**, e2023JC020565 (2024).
51. Landry, M. R., Freibott, A. L., Beatty, J. L. & Selph, K. E. Phytoplankton biomass responses to a marine heat wave align with altered nitracline depth. *Limnol. Oceanogr.* **69**, 1683–1694 (2024).
52. Rykaczewski R. R. & Dunne J. P. Enhanced nutrient supply to the California Current Ecosystem with global warming and increased stratification in an Earth System Model. *Geophys. Res. Lett.* **37**, (2010).
53. Amaya, D. J., Alexander, M. A., Scott, J. D. & Jacox, M. G. An evaluation of high-resolution ocean reanalyses in the California current system. *Prog. Oceanogr.* **210**, 102951 (2023).
54. Alexander, M. A. et al. A survey of coastal conditions around the continental US using a high-resolution ocean reanalysis. *Prog. Oceanogr.* **216**, 103055 (2023).
55. Zaba, K. D. & Rudnick, D. L. The 2014–2015 warming anomaly in the Southern California Current System observed by underwater gliders. *Geophys. Res. Lett.* **43**, 1241–1248 (2016).
56. Zheng, J. et al. Phytoplankton response to the record-breaking marine heatwave in the summer of 2020 in the South China Sea. *J. Geophys. Res.: Oceans* **129**, e2024JC021275 (2024).
57. Beckmann, A. & Hense, I. Beneath the surface: Characteristics of oceanic ecosystems under weak mixing conditions—A theoretical investigation. *Prog. Oceanogr.* **75**, 771–796 (2007).
58. Kavanaugh, M. T. et al. Experimental assessment of the effects of shade on an intertidal kelp: do phytoplankton blooms inhibit growth of open coast macroalgae?. *Limnol. Oceanogr.* **54**, 276–288 (2009).
59. Shigesada, N. & Okubo, A. Analysis of the self-shading effect on algal vertical distribution in natural waters. *J. Math. Biol.* **12**, 311–326 (1981).
60. Moreira-Coello, V. et al. Biological N2 fixation in the upwelling region off NW Iberia: magnitude, relevance, and players. *Front. Mar. Sci.* **4**, 303 (2017).
61. Mouriño-Carballedo, B. et al. Magnitude of nitrate turbulent diffusion in contrasting marine environments. *Sci. Rep.* **11**, 18804 (2021).
62. Myers, T. A., Mechoso, C. R., Cesana, G. V., DeFlorio, M. J. & Waliser, D. E. Cloud feedback key to marine heatwave off Baja California. *Geophys. Res. Lett.* **45**, 4345–4352 (2018).

63. Cloern, J. E. The relative importance of light and nutrient limitation of phytoplankton growth: a simple index of coastal ecosystem sensitivity to nutrient enrichment. *Aquat. Ecol.* **33**, 3–15 (1999).
64. Shiozaki, T. et al. Bottom-associated phytoplankton bloom and its expansion in the Arctic Ocean. *Glob. Change Biol.* **28**, 7286–7295 (2022).
65. Hu, Q. et al. Seasonal variability of phytoplankton biomass revealed by satellite and BGC-Argo data in the central tropical Indian Ocean. *J. Geophys. Res.: Oceans* **127**, e2021JC018227 (2022).
66. Gomes, D. G. et al. An updated end-to-end ecosystem model of the northern California Current reflecting ecosystem changes due to recent marine heatwaves. *PLoS One* **19**, e0280366 (2024).
67. Iglesias, I. S., Fiechter, J., Santora, J. A. & Field, J. C. Vertical distribution of mesopelagic fishes deepens during marine heatwave in the California Current. *ICES J. Mar. Sci.* **81**, 1837–1849 (2024).
68. Ohman, M. D. et al. Ecological transitions in a coastal upwelling ecosystem. *Oceanography* **26**, 210–219 (2013).
69. Franks, P. J. et al. Modeling physical-biological responses to climate change in the California Current System. *Oceanography* **26**, 26–33 (2013).
70. Cordero-Quirós, N. et al. Physical-ecological response of the California current system to ENSO events in ROMS-NEMURO. *Ocean Dyn.* **72**, 21–36 (2022).
71. Cordero-Quirós, N., Miller, A. J., Subramanian, A. C., Luo, J. Y. & Capotondi, A. Composite physical-biological El Niño and La Niña conditions in the California Current System in CESM1-POP2-BEC. *Ocean Model.* **142**, 101439 (2019).
72. Miller, A. J., Song, H. & Subramanian, A. C. The physical oceanographic environment during the CCE-LTER Years: Changes in climate and concepts. *Deep Sea Res. Part II: Top. Stud. Oceanogr.* **112**, 6–17 (2015).
73. Mélin F. et al. Global trends in chlorophyll concentration observed with the satellite ocean colour data record. In: *Living Planet Symposium* (2016).
74. Stone, H. B., Banas, N. S., MacCready, P., Kudela, R. M. & Oval, B. Linking chlorophyll concentration and wind patterns using satellite data in the central and northern California current system. *Front. Mar. Sci.* **7**, 551562 (2020).
75. Aumont, O., Éthé, C., Tagliabue, A., Bopp, L. & Gehlen, M. PISCES-v2: an ocean biogeochemical model for carbon and ecosystem studies. *Geosci. Model Dev. Discuss.* **8**, 1375–1509 (2015).
76. Reynolds, R. W. et al. Daily high-resolution-blended analyses for sea surface temperature. *J. Clim.* **20**, 5473–5496 (2007).
77. Smith, K. E. et al. Baseline matters: Challenges and implications of different marine heatwave baselines. *Prog. Oceanogr.* **231**, 103404 (2025).
78. Liang, S. & Wang, D. Moderate resolution imaging spectroradiometer (MODIS) downward shortwave radiation (MCD18A1) and photosynthetically active radiation (MCD18A2) algorithm theoretical basis document. In: *Google Scholar, There is no Corresponding Record for This Reference*, (2017).
79. Lengaigne, M. et al. Influence of the oceanic biology on the tropical Pacific climate in a coupled general circulation model. *Clim. Dyn.* **28**, 503–516 (2007).

## Acknowledgements

We thank our numerous colleagues and the shipboard operations crews in the CalCOFI and CCE LTER Programs whose decades of work made this

study possible. This research was supported by National Science Foundation grant OCE-2224726 to the CCE LTER Program, National Key R&D Program of China (Grant No. 2022-34), Scientific and technological projects of Zhoushan (Grant No. 2022C01004) and National Natural Science Foundation of China (No. 42576028). We thank the three anonymous referees for their very constructive comments.

## Author contributions

J.L. and A.M designed the study. J.L. conducted the analyses and wrote the first draft of the manuscript under A.M. and P.B.'s instruction. D.A. and Q.W. were involved in improving the manuscript. Y.G. and P.L. contributed to the discussion and revision of the study.

## Competing interests

The authors declare no competing interests.

## Additional information

**Supplementary information** The online version contains supplementary material available at <https://doi.org/10.1038/s43247-025-02835-8>.

**Correspondence** and requests for materials should be addressed to Yanzhen Gu or Peng Bai.

**Peer review information** *Communications Earth & Environment* thanks Craig G. Gelpi, Kyung-Min Noh and the other, anonymous, reviewer(s) for their contribution to the peer review of this work. Primary Handling Editors: José Luis Iriarte Machuca and Alice Drinkwater. A peer review file is available.

**Reprints and permissions information** is available at <http://www.nature.com/reprints>

**Publisher's note** Springer Nature remains neutral with regard to jurisdictional claims in published maps and institutional affiliations.

**Open Access** This article is licensed under a Creative Commons Attribution-NonCommercial-NoDerivatives 4.0 International License, which permits any non-commercial use, sharing, distribution and reproduction in any medium or format, as long as you give appropriate credit to the original author(s) and the source, provide a link to the Creative Commons licence, and indicate if you modified the licensed material. You do not have permission under this licence to share adapted material derived from this article or parts of it. The images or other third party material in this article are included in the article's Creative Commons licence, unless indicated otherwise in a credit line to the material. If material is not included in the article's Creative Commons licence and your intended use is not permitted by statutory regulation or exceeds the permitted use, you will need to obtain permission directly from the copyright holder. To view a copy of this licence, visit <http://creativecommons.org/licenses/by-nc-nd/4.0/>.

© The Author(s) 2025